Balaguer Ramirez, M.; Solis Díaz, C.; Serra Alfaro, JM. (2011). Study of the transport properties of the mixed ionic electronic conductor Ce 1-x Tb x O 2- + Co (x=0.1, 0.2) and evaluation as oxygen-transport membrane. Chemistry of Materials. 23(9):2333-2343. doi:10.1021/cm103581w

Study of the transport properties of the mixed ionic electronic conductor $Ce_{1-x}Tb_xO_{2-\delta}$ + Co (x=0.1, 0.2) and evaluation as oxygen-transport membrane

*María Balaguer, Cecilia Solís, José M. Serra**

Instituto de Tecnología Química (Universidad Politécnica de Valencia – Consejo Superior de Investigaciones Científicas), Av. Naranjos s/n, E-46022 Valencia (SPAIN)

TITLE RUNNING HEAD: mixed ionic electronic conductivity of $Ce_{1-x}Tb_xO_{2-\delta}$ + Co (x=0.1, 0.2) as oxygen-transport membrane

* to whom correspondence should be addressed, Fax 0034.963.877.809

e-mail: jmserra@itq.upv.es

Chemistry of Materials 23 (2011) 2333-2343

(doi:10.1021/cm103581w)

ABSTRACT:

Tb doped ceria materials have been synthesized by coprecipitation method. Cobalt oxide (2 mol%) has been added in order to improve the sinterability and conductivity. XRD measurements suggest that a part of the cobalt is incorporated in the ceria lattice. $Ce_{1-x}Tb_xO_{2-\delta}$ materials showed predominantly ionic conductivity, but the mixed ionic electronic conductivity can be tuned by modifying Tb and Co doping level and temperature range. The ambipolar conductivity was determined by galvanic method coupled with gas permeation and these results support the applicability of these materials as oxygen transport membranes at high temperature. $Ce_{1-x}Tb_xO_{2-\delta}$ +Co membranes are CO_2 stable and yielded oxygen fluxes that can compete with reported perovskite materials. Oxygen diffusion and surface exchange coefficients in the range 10^{-5} - 10^{-4} cm^2/s and 10^{-4} - 10^{-3} cm/s from 773-1023 K have been obtained by conductivity relaxation.

KEYWORDS**:** Mixed ionic electronic conductor, nanocrystalline oxide, fuel cell, oxygen permeation membrane, $Ce_{1-x}Tb_xO_{2-\delta}$, doped ceria, conductivity relaxation

BRIEFS: Mixed-conducting materials for *in situ* separation of oxygen at high temperatures applicable as oxygen transport membrane.

Study of the transport properties of the mixed ionic electronic conductor $Ce_{1-x}Tb_xO_{2-\delta}$ + Co (x=0.1, 0.2) and evaluation as oxygen-transport membrane

1. Introduction

Oxygen production at high temperature through ceramic membranes represents a current challenge that would enable the introduction of more efficient and environmental-friendly power generation and chemical production processes. In fact, reliable mass-scale O_2 separation in membrane modules would allow the cost-effective operation of *Oxyfuel* power plants [1], which can integrate CO_2 capture and sequestration strategies in order to minimize CO_2 emissions. Oxyfuel combustion principle is the removal of nitrogen from the oxidizer to carry out the combustion process in an oxygen-enriched gas stream, thus reducing gas volume and recycling the flue gas to lower the flame temperature. Hence, an air separation unit (ASU) has to be added to the power plant. The current state of technology development for ASU applies high energy consuming cryogenic distillation units while alternative oxygen separation technologies such as ion transport membranes [2] would enable thermal integration and energy savings. Furthermore, several chemical processes [3,4,5,6,7] would benefit from the development of highly-permeable and CO_2 stable ceramic membranes, since it would make possible the process intensification and the improvement of product selectivity by avoiding the direct contact of molecular oxygen and reaction products.

Membranes based on mixed ionic electronic conductor (MIEC) materials [8,9] enable *in situ* separation of oxygen in a membrane reactor fed by air. The most common type of material that exhibits both ion and electron conducting properties are perovskites e.g. $Ba_{1-x}Sr_xCo_{0.8}Fe_{0.2}O_{3-\delta}$ (BSCF), $La_{1-x}Sr_xCo_{0.8}Fe_{0.2}O_{3-\delta}$ (LSCF), which are thermally stable [10] and enable to achieve oxygen fluxes of 6 $ml \cdot cm^{-2} min^{-1}$ (BSCF) and 3.2 $ml \cdot cm^{-2} min^{-1}$ (LSFC) at 1173 K using argon as sweep gas [11,12]. BSCF hollow fibre configuration improves fluxes up to 9.5 $ml \cdot cm^{-2} min^{-1}$ at 1223 K [13, 14]. However, the main disadvantage of these materials is the limited chemical stability under a large oxygen concentration gradient, with one side of the membrane exposed to air oxidizing atmosphere and the other side to reducing or CO_2 containing atmosphere [15,16,17]. Even at 300 ppm [18], CO_2 presence is a major issue for perovskite-based membranes (e.g. BSCF) due to the carbonation reaction of the earth alkali metals included in their structure.

Lanthanide substituted ceria materials show a particular combination of high oxygen-ion mobility, redox catalytic properties and chemical compatibility with water and carbon dioxide at high temperatures. In addition, it shows n-type electronic conductivity due to the partial reduction of the cerium ion from the tetravalent to the trivalent state at high temperatures under reducing conditions. Namely, the electron transport takes place by hopping between cerium sites via a small polaron process. By doping with multivalent cations, mixed conduction in ceria may be further extended to higher oxygen partial pressure range (10^{-5}-10^{-1} atm), which enables its application as oxygen permeable membranes. Terbium and praseodymium fulfil the multivalence condition. Fagg et al.[19] developed cobalt-doped $Ce_{0.8}Pr_{0.2}O_{2-\delta}$ membranes that offer competitive levels of oxygen permeation flux at temperatures below 1123 K when compared with perovskite materials. Chatzichristodoulou et al. have co-doped Pr doped ceria with Tb and concluded that high non-stoichiometry and oxidation state of both elements depends on the relative amount of the two dopants [20,31]. Another strategy for reaching mixed ionic and electronic conductivity is the fabrication of composites to combine the ionic properties of a doped ceria with a primarily electronic material, e.g. $Ce_{0.8}Gd_{0.2}O_{2-\delta}$ (CGO) combined with $La_{0.7}Sr_{0.3}MnO_{3-\delta}$.(LSM) or $La_{0.8}Sr_{0.2}Fe_{0.8}Co_{0.2}O_{3-\delta}$.(LSFC) [21]. Nevertheless, the interaction of properties was found to be detrimental for the total conductivity and oxygen permeability.

In this work, four different compositions based on undoped and cobalt-doped $Ce_{1-x}Tb_xO_{2-\delta}$ have been prepared and structurally characterized in order to clear up the electrochemical behavior and oxidation state of terbium doped ceria. Total conductivity measurements in high pO_2 range combined with temperature programmed desorption and reduction enabled to gain insight into the conduction mechanisms dependent on pO_2 and temperature. Subsequently, conductivity relaxation, CO_2 stability and oxygen permeation and ion pumping experiments were done to assess the applicability of this kind of materials in oxygen separation and catalytic membrane reactors.

2. Experimental

Terbium doped ceria has been prepared by co-precipitation method in order to synthesize powders of nanometric size. This technique consists of the dissolution of commercial lanthanide nitrates mixture in distilled water at 323 K. $NH_3(NH_4)_2CO_3$ solution in a 1:1.5 molar ratio was dropped under stirring into the lanthanides solution to achieve the total precipitation. The resulting precursor powder was dried at 373 K after filtration and rinsing. Cobalt incorporation (when required) was done over the dried precursor powder by incipient wetness impregnation. Calculated 2% molar of Co was dissolved in distilled water (volume corresponding to the pore volume) and mixed with the powder. Finally, each powder was calcined during 5 hours in air atmosphere at 1073 K to decompose the residual nitrates and carbonates and to favor the formation of the fluorite phase.

In order to identify the crystalline phase(s) and determine crystallite size and lattice parameters of the samples, the powders were characterized by X-ray diffraction (XRD). The measurements were carried out by a PANalytical X'Pert PRO diffractometer, using $CuK\alpha_{1,2}$ radiation and an X'Celerator detector in Bragg-Brentano geometry. The studies of the thermal behavior of the material were performed in an Anton Paar XRK-900 reaction chamber attached to the diffractometer, either in a dry air atmosphere or in helium up to 1173 K. XRD patterns were recorded in the 2θ range from 0º to 90º and analyzed using X'Pert Highscore Plus software. The lattice parameters were calculated by using the equation for a cubic system:

$$a = d\sqrt{h^2 + k^2 + l^2} \qquad (1)$$

Where h, k and l are the Miller indexes, d is de inter-plane distance calculated from the Bragg's law: $2d\sin\theta = n\lambda$, being λ=1.5406 Å the $K_{\alpha 1}$ wavelength of the Cu, θ the scattering angle and n the integer representing the order of the diffraction peak. The particle size has been also extracted from XRD patterns taking into account that the width of the peaks is influenced by the size of the particles [22]. Then from the Scherrer formula:

$$\beta_{size} = \frac{0.9\lambda}{t\cos\theta} \qquad (2)$$

Where β is the full width at half maximum (FWHM) of the XRD peak and t is the average crystal size. In this study the lattice parameter (a) and the particle size (t) have been calculated from the 2θ position and the FWHM of (0 2 2) and (4 2 2) peaks respectively, extracted by fitting with a Gaussian [22].

Temperature programmed desorption (TPD) measurements were performed in order to observe the oxygen release with temperature. The powdery material (100 mg) sintered at 1473 K was placed in a quartz reactor and it was heated up in air up to it 1273K and cooled down in the same atmosphere. Then the sample was heated up at 10 K/min up to 1273K in He and the oxygen release was monitored by following the m/z = 32 and 16 amu with a mass spectrometer Omnistar (Balzers).

Micromeritics system was used to carry out temperature-programmed reduction (TPR). Thus, 100 mg of sample was degassed under Ar flow for 1 h and then was subjected to reduction under H_2/Ar (1/9) flow, and heating rate of 10 K/min till 1273 K. The H_2 consumption was measured by a TCD. Thermogravimetry analysis was performed on a Mettler-Toledo StarE equipment in air with 5% CO_2 and using a heating ramp of 10 K/min.

Rectangular probes (4 x 0.4 x 0.2 cm^3) of the powders fired at 1073 K were uniaxially pressed at 125 MPa during 1 minute and subsequently sintered 5 hours at 1573 K in air atmosphere. Electrical conductivity measurements were conducted by standard four-point DC technique on the sintered rectangular bars using silver wire and paste for contacting. The measurements were carried out in a temperature range from 673 to 1073 K by cooling down (1 K/min) in constant atmospheres under different O_2 contained atmospheres. The constant current was supplied by a programmable current source (Keithley 2601) and the voltage drop through the sample was detected by a multimeter (Keithley 3706). The conductivity measurements are thermally activated and are analysed on the basis of Arrhenius behaviour $\sigma(T) = (A/T)\ exp(-E_a/kT)$. The activation energy E_a has been extracted from the slope of the graphs. Once the highest temperature (1273K) is reached, the samples are let stabilize during two hours in order to warrantee the high-temperature reduction state corresponding to the specific pO_2.

Permeation and transport numbers measurements were performed on 15 mm diameter disks. The sample consisted of a gastight $Ce_{1-x}Tb_xO_{2-\delta}$ + Co (2 mol%) disc

sintered at 1473 K. Sealing was done by using gold gaskets. Oxygen was separated from air (65 mL/min) using 200 mL/min argon as sweep gas. Permeate was analyzed using a micro-GC Varian CP-4900 equipped with Molsieve5A, PoraPlot-Q glass capillary, and CP-Sil modules. Transport numbers were calculated from the oxygen permeation deviation of pure ionic behavior when an input current from 0 to 75 mA was imposed using a Solartron 1470E equipment.

The electrical conductivity relaxation technique (ECR) was carried out in a tubular oven in which the gas volume was minimized in order to achieve an almost instantaneous pO_2 change. The same four-point DC technique was used to monitor the electrical conductivity, but the thickness of the probe was reduced to obtain shorter relaxation times. The oxygen exchange kinetics was investigated by alternatively swapping oxygen partial pressure from 1 to 0.21 atm at some given temperatures. *D* and *k* are determined by fitting the appropriate solution of the Fick's diffusion equation [23,24] to the experimental relaxation curves of the electrical conductivity plotted in Figure 6a,

$$\frac{\sigma-\sigma_0}{\sigma_\infty-\sigma_0}=1-\left[\sum_{m=1}^{\infty}\frac{2L_x^2}{\beta_{m,x}^2\left(\beta_{m,x}^2+L_x^2+L_x\right)}\exp\left(\frac{-\beta_{m,x}^2 Dt}{l_x^2}\right)\times\sum_{n=1}^{\infty}\frac{2L_y^2}{\beta_{n,y}^2\left(\beta_{n,y}^2+L_y^2+Ly\right)}\exp\left(\frac{-\beta_{n,y}^2 Dt}{l_y^2}\right)\times\right.$$
$$\left.\times\sum_{p=1}^{\infty}\frac{2L_z^2}{\beta_{p,z}^2\left(\beta_{p,z}^2+L_z^2+L_z\right)}\exp\left(\frac{-\beta_{p,z}^2 Dt}{l_z^2}\right)\right] \quad (3)$$

where *x*, *y*, *z* are the sample dimensions, *t* the time in seconds and $L_x=\beta_{m,x}\tan\beta_{m,x}\equiv\frac{l_x k}{D}$, $L_y=\beta_{n,y}\tan\beta_{n,y}\equiv\frac{l_y k}{D}$, $L_z=\beta_{p,z}\tan\beta_{p,z}\equiv\frac{l_z k}{D}$ being l_i half of each sample dimension.

Once the electrochemical analysis was done, cross-sections of the sintered probes were analyzed by SEM and EDX using a JEOL JSM6300 electron microscope.

3. Results and discussion

3.1. Structural characterization

XRD patterns of $Ce_{1-x}Tb_xO_{2-\delta}$ and $Ce_{1-x}Tb_xO_{2-\delta}$ + Co (2 mol%) sintered at 1573 K are shown in Figure 1. All the powders are single cubic fluorite structured with space group Fm3m. Diffraction peaks corresponding to any precursor or secondary phase were not observed. The obtained patterns indicate that terbium forms a solid solution

and incorporates in the lattice of ceria as both compositions are below the solubility limit of Tb in ceria compounds [25,29]. As previously reported [26], cobalt acts as a sintering aid and enables lowering the densification temperature. Co-containing samples show sharper and more intense diffraction peaks as a consequence of the grain size growth. No secondary phases related to Co were detected by XRD.

SEM pictures of $Ce_{0.9}Tb_{0.1}O_{2-\delta}$ and $Ce_{0.9}Tb_{0.1}O_{2-\delta}$ + Co 2% membranes calcined at 1473 K showed in Figure 1, confirm the grain size growth [27]. EDS did not prove the presence of Co in any preferential location, e.g., in the grain boundary as reported for other doped cerias.

As no secondary crystalline phases appeared to the limit of XRD, the lattice parameter should follow the Vegard's rule, i.e., a linear relationship exists between cell parameter and the concentration of the solute or dopant [28,29],

$$a = 5.4113 + \frac{4}{\sqrt{3}}[r_M - 1.024]\cdot x \qquad (4)$$

where r_M is the ionic radius of the dopant cation and x is the dopant amount in $Ce_{1-x}Tb_xO_{2-\delta}$.

Figure 2a depicts the cell parameter measured at room temperature as a function of the amount of Tb (x=0, 0.1, 0.2) for Co-free and -containing series. The slope of this line is known as Vegard's slope. First it can be appreciated that Co-containing compounds have a slightly shorter cell parameter than Co-free samples. This can be attributed to the partial incorporation of Co cations into the ceria lattice while the rest should be in the grain boundary. Specifically, an incorporation of 1.3 mol% of Co^{+2} [30] would give rise to the cell parameter change observed in CeO_2.

The dashed lines in Figure 2a correspond to the theoretical Vegard's slope [28] for both oxidation states[1], Tb^{3+} and Tb^{4+}, and the corresponding with a constant incorporation of 1.3 mol% Co. No change in the oxidation state of Ce cations is assumed. The experimental results lay inside the defined theoretical limits and the lattice parameter decreases with the amount of Tb. For each series, the cell parameter in oxidizing atmospheres and at room temperature follows a nearly linear trend and this means that the ratio Tb^{+4}/Tb remains constant in the studied Tb concentration range.

[1] Taking into account that the ionic radii of Ce^{4+}, Ce^{3+}, Tb^{4+}, Tb^{3+} and Co^{2+} in eight-fold coordination are 0.97, 1.143, 0.88, 1.04 and 0.90 Å respectively.

Considering the theoretical and experimental slopes for Co-free (solid circles) and Co-containing compounds (open circles), a rough estimation of the Tb^{+4}/Tb proportion at room temperature can be done, i.e., 38% (Co-free) and 48% (Co-containing). The first value agrees with that obtained by Chatzichristodoulou et al. for $Ce_{0.8}Tb_{0.2}O_{2-\delta}$ measured by XANES [31]. Moreover, the Co addition allows increasing the Vegard's slope, i.e., it produces a slight decrease in the cell parameter, when compared to Co-free samples, and this is an indication of the higher oxidation state in the Co containing compounds. It should be pointed out that a higher amount of incorporated Co in the lattice cannot explain such high cell parameter shrinkage of the $Ce_{0.8}Tb_{0.2}O_{2-\delta}$ sample that would need to incorporate almost twice the Co nominally available. Otherwise, it is well-known that cobalt cations/species have high redox activity and this enables to increase the reduction and re-oxidation rate of bulk material. The improved reduction activity of cobalt has been studied by temperature programmed oxygen desorption (TPD) in helium and temperature programmed reduction (TPR) in hydrogen. TPR measurements confirm that there is a higher reducibility of Tb^{4+} to Tb^{3+} in specimens containing Co, which present greater consumption of H_2 (see Figure S1).

The evolution of the cell parameter with different compositions also agrees with the evolution of grain size of the samples calculated by Scherrer equation (2). Figure 2b shows that 10% Tb doped samples have a larger cell parameter and smaller grain sizes. This lattice expansion with decreasing grain size at room temperature is due to the larger concentration of oxygen vacancies associated to the presence of intrinsic defects of Ce^{3+} and/or Tb^{3+} as previously reported for other cerias [32,33, 34].

Room temperature XRD results of as sintered samples cannot be extrapolated to operating conditions due to different redox processes dependent on temperature and pO_2. In order to check the evolution of cell parameters and associated vacancy concentration at high temperature, XRD measurements were performed on $Ce_{0.9}Tb_{0.1}O_{2-\delta}$ by heating the specimen in air up to 1173 K and cooling it down in helium. The results plotted in Figure 3 show a linear dependency of cell parameter with temperature and an increase of the slope at 700 K, once proved that fluorite structure is maintained in the whole temperature range. The first slope corresponds to the thermal expansion coefficient (12.1×10^{-6} K^{-1}) in air. Above 700 K, the increase in slope can be interpreted as the additional contribution of chemical expansion due to the reduction of Tb^{+4} to Tb^{+3} and the associated oxygen release. From these results, a linear chemical expansion

coefficient can be estimated ($5.77x10^{-6}$ K^{-1}) for the temperature range from 700 to 1173 K. When the sample is cooled down in He, the material cannot be re-oxidized due to the lack of molecular oxygen necessary for re-oxidation, and only thermal expansion can be observed for the material in *reduced* state. It should be noted that the linear thermal expansion coefficient coincides for the oxidized and reduced material. Indeed, this value is very similar to that obtained for $Ce_{0.9}Gd_{0.1}O_{2-\delta}$ (Figure 3), which shows neither chemical expansion nor oxygen release in the studied pO_2 range.

The oxygen release is confirmed by TPD measurements for all samples, as depicted in Figure 4, where the ion current corresponding to the released oxygen from the solid is plotted as a function of temperature. $Ce_{0.9}Tb_{0.1}O_{2-\delta}$ oxygen desorption starts at ~700 K, approximately the same temperature at which the chemical expansion becomes tangible by HT-XRD. It reaches a maximum at 755 K and decreases hereafter. This oxygen release suggests the reduction of the material through the concurrent cation reduction and oxygen vacancy formation. However, the non-stoichiometry of ceria and doped ceria materials has been exhaustively studied [31,35,36,37] demonstrating that Ce^{4+} reduction initiates at oxygen partial pressures lower than 10^{-10} atm and keeps nearly constant at higher oxygen contents. Consequently, in the present study, the changes in oxygen non-stoichiometry observed at the most oxidizing conditions ($>10^{-5}$ atm) are most likely related to the reduction of Tb^{4+} /Tb^{3+} rather than Ce^{4+}.

For $Ce_{0.8}Tb_{0.2}O_{2-\delta}$ and Co-containing samples, a more complex reduction behavior can be ascertained, i.e., two main redox processes can be distinguished (Figure 4): (1) the oxygen release related to Tb^{4+} reduction starts at lower temperatures, i.e. ca. 600 K for both Co added samples, with respect to the Co-free samples; and (2) a new important well-defined reduction process takes place at temperatures ranging from 1000 to 1150 K and it reaches a maximum at 1010 K, 1050 K and 1070 K for $Ce_{0.8}Tb_{0.2}O_{2-\delta}$, $Ce_{0.9}Tb_{0.1}O_{2-\delta}$ + Co 2% and $Ce_{0.8}Tb_{0.2}O_{2-\delta}$+ Co 2%, respectively. This new high-temperature reduction process can be ascribed to different processes:

(i) the reduction of Co itself ($Co^{3+} \rightarrow Co^{2+}$)[30] confirmed by the existence of this reduction in in $CeO_{2-\delta}$ +Co sample, and not present in $CeO_{2-\delta}$ as shown in the inset of Figure 4.

(ii) further reduction of bulk Tb^{4+} to Tb^{3+} confirmed by the existence of a broad second reduction peak in $Ce_{0.8}Tb_{0.2}O_{2-\delta}$ sample (without Co but with a higher concentration of reducible Tb^{+4}).

In summary, TPD measurements demonstrate that the addition of either Co or a higher amount Tb allows increasing the oxygen release, i.e., the material reducibility. By taking $Ce_{0.9}Tb_{0.1}O_{2-\delta}$ oxygen desorption as reference, it is possible to determine quantitatively the relative impact of the changes in the oxide composition. 20% Tb doping enables an increment of 1% ascribed to a higher reduction degree of Tb^{4+} to Tb^{3+}, as also suggested by TPR measurements (supporting figure S1). The addition of Co in $Ce_{0.9}Tb_{0.1}O_{2-\delta}$ sample results in a 6.4% increase in the oxygen desorption and this is attributed to the Co reduction itself and the enhancement of Tb^{+4} reduction (broad peak at around 765 K). Finally, Co addition to $Ce_{0.8}Tb_{0.2}O_{2-\delta}$ sample leads to the highest oxygen release, 7.7% with respect to reference sample.

3.2.Conductivity and transport number measurements

Figure 5 shows the conductivity $\ln(\sigma T)$ as a function of the reverse temperature for all compositions of terbium doped ceria measured in pO_2 of 0.21 and $5x10^{-5}$ atm. Given a sample composition, differences in conductivity at different pO_2 would indicate a change in the level of reduction. Moreover, oxygen can be more easily incorporated at high pO_2 as temperature drops while it cannot be incorporated (reoxidization) at low pO_2. This is translated into an apparent change in activation energy (E_a) under oxidizing atmospheres (1 and 0.21 atm) while reoxidization cannot be observed at $5x10^{-5}$ atm in the measured temperature range (1073-673 K). The variations in E_a at given conditions indicate a temperature dependent change in the conductivity behaviour of the material. Taking into account that at these high pO_2 atmospheres doped ceria materials have been reported as pure ionic conductors, the change in apparent E_a could be analyzed in terms of vacancy concentration increase due to the release of oxygen (Tb reduction). Actually, E_a change of $Ce_{0.9}Tb_{0.1}O_{2-\delta}$ in air is produced at 740-750 K, which matches the temperature range reported by XRD for oxygen desorption/incorporation (Figure 3) and TPD (Figure 4).

Table 1 summarizes apparent E_a in the temperature ranges of 1073-750 K and 750-673 K and the conductivity at 1073 K under 0.21 and $5x10^{-5}$ atm pO_2. Experimental E_a match the typical values found for ionic conductors. At pO_2 lower than 10^{-3} atm, there exists only one E_a for all compositions, i.e., terbium is mainly reduced to Tb^{+3}, over the whole studied temperature range, thus behaving as a fixed valence dopant, which enhances principally the ionic conductivity.

The increase from 10 to 20% of Tb and the addition of cobalt enables increasing substantially the total conductivity and the best conductivity values have been obtained for $Ce_{0.8}Tb_{0.2}O_{2-\delta}$ + Co 2%. Firstly, the behaviour of Co-free $Ce_{1-x}Tb_xO_{2-\delta}$ samples is discussed. Taking into account that the studied range of pO_2 only includes the region of dopant reduction ($Tb^{+4} \rightarrow Tb^{3+}$) [31], the increase of Tb should give rise to a higher concentration of oxygen vacancies with the corresponding raise in ionic conductivity. As shown in Table 1, conductivity of $Ce_{0.8}Tb_{0.2}O_{2-\delta}$ in air at 1073 K is twice the conductivity of $Ce_{0.9}Tb_{0.1}O_{2-\delta}$ which confirms the previous observations, i.e., conductivity is mainly ionic in these oxidizing conditions and the multiple oxidation state of the dopant makes the ionic conductivity pO_2 dependent (region not observed in single-oxidation-state acceptor doped systems as Gd).

When Co is added to both compositions, reducibility of the sample is enhanced as shown in TPD (Figure 4) and TPR measurements (Figure S1). This allows the oxygen vacancy concentration to be higher at the same temperature with respect to the Co-free samples. This makes it possible to increase the ionic conductivity and promote electronic conduction as it is confirmed later on by oxygen permeation results.

The apparent E_a values observed for the different samples (Table 1) are intermediate values between the E_a ones corresponding to the major conduction processes contributing to the total conductivity. Therefore, changes in the E_a in this kind of mixed conducting materials are ascribed to the variation in the proportion between ionic and electronic contributions. The E_a decrease in 10% Tb doped material when Co is added is attributed to a rise in electronic conductivity. In 20% doped samples the amount of Tb is high enough to allow small polaron hopping and the material becomes a mixed conductor. The introduction of Co promotes the formation of new oxygen vacancies and this causes an increase in E_a due to the higher ionic conductivity.

$Ce_{0.8}Tb_{0.2}O_{2-\delta}$ + Co transference numbers were obtained across a 1.2 mm thick membrane under a pO_2 gradient $0.21/5x10^{-5}$ atm (air/Ar). Figure 6a presents the ionic, electronic and total conductivity values obtained from transference numbers showed in Figure 6b. This study was performed in the temperature range from 1023 to 1293 K suitable for application as oxygen transport membranes. The results confirm the mixed ionic-electronic conductivity of this composition. Ionic conductivity is predominant in the whole temperature range but electronic contribution becomes more important as the temperature drops.

In order to analyze the complete conductivity mechanism in the studied range of temperatures and pO_2 it would be necessary to explore the defect chemistry of these compounds. The dominant defect equilibrium at high pO_2 in the system $Ce_{1-x}Tb_xO_{2-\delta}$ is thereby suggested to be that of Tb reduction. Stefanik and Tuller [38] and Fagg et al [35] described a defect model including a variable valency acceptor dopant. The main key defect reactions are listed below, starting with the consideration of pure CeO_2.

First, the formation of oxygen vacancies and interstitials is dominated by the Frenkel defect mechanism for pure CeO_2 as described in (5) while intrinsic electron-hole pair generation provoked by thermal excitation over the band gap is governed by (6). On the other hand, molecular oxygen release and oxygen vacancy generation (charge compensated by the formation of free electrons localized on Ce ions) and hopping conduction, will occur over the Ce^{3+}/Ce^{4+} from intrinsic defects of pure ceria sublattice following (7).

$$O_O^{\times} \rightarrow V_O^{\cdot\cdot} + O_i'' \; ; \quad [V_O^{\cdot\cdot}]\,[O_i''] = K_F(T) \tag{5}$$

$$nil = e' + h^{\cdot} \; ; \quad np = K_e(T) \tag{6}$$

$$O_O^{\times} \rightarrow \frac{1}{2}O_2\,(g) + V_O^{\cdot\cdot} + 2e' \; ; \quad [V_O^{\cdot\cdot}]n^2\,pO_2^{1/2} = K_R(T) \tag{7}$$

In a Tb doped system it has to be taken into account the mass conservation law (8), the ionization of Tb cations (9), and the added charge defect Tb'_{Ce} in order to keep the electroneutrality condition (10).

$$[Tb'_{Ce}] + [Tb_{Ce}^{\times}] = Tb_{total} \tag{8}$$

$$Tb'_{Ce} \rightarrow Tb_{Ce}^{\times} + e' \; ; \quad \frac{[Tb_{Ce}^{\times}]n}{[Tb'_{Ce}]} = K_{Tb}(T) \tag{9}$$

$$2\left[O_i^{''}\right] + n + \left[Tb_{Ce}^{'}\right] = 2[V_O^{\cdot\cdot}] + p \tag{10}$$

As Tb enhances the overall reduction in the material, the concentration of oxygen vacancies will be high. Hence, the concentration of interstitial oxygen will be suppressed $\left[O_i^{''}\right] \rightarrow 0$, improving the ionic conductivity over p-type electronic conductivity in the high pO_2 range, i.e., $p \rightarrow 0$ in eq. (10). Besides, in oxidizing conditions and low temperatures (below 750 K) most terbium exists as Tb^{4+} and then $Tb'_{Ce} << Tb_{Ce}^{\times}$ ($n << K_{Tb}$). Then:

$$n \propto pO_2^{-1/6} \tag{11}$$

$$[V_O^{\cdot\cdot}] \propto pO_2^{-1/6} \quad (12)$$

In the case when $Tb'_{Ce} >> Tb^{\times}_{Ce}$ (n >> K_{Tb}) but Tb_{total} >> n; consequently:

$$n \propto pO_2^{-1/4} \quad (13)$$

$$[V_O^{\cdot\cdot}] \propto pO_2^{0} \quad (14)$$

Thus vacancy concentration is independent on pO_2 and proportional to the total terbium concentration.

When Co is added it seems, from XRD analysis, that is partially incorporated in the lattice as Co^{2+} following similar equation as Tb but giving rise to one oxygen vacancy per substituted Ce [30]. Therefore the electroneutrality balance equation (10) must be modified with the addition of $\left[Co''_{Ce}\right]$ in the left term. The rest of Co is likely placed along the grain boundaries and does not affect bulk defect chemistry in equilibrium.

Equations above describe a way to make an evaluation of the predominant type of carries from the conductivity behavior with pO_2. Figure 7 plots the conductivity logarithm at 673 K (a) and 1073 K (b) versus pO_2 logarithm for the different compositions.

At 673 K, over the whole range of pO_2, $Ce_{0.9}Tb_{0.1}O_{2-\delta}$ show -1/6 dependency, which could be characteristic of both n-type electronic conductivity and ionic conductivity for this material and conditions, as described by eq. (11) and (12) respectively. At 1073 K the -1/6 dependency exists but there is a conductivity plateau at pO_2 lower that 10^{-3} atm, characteristic of ionic transport as illustrated in eq. (14). This plateau should be related to a maximum reduction of Tb reachable at these temperatures in this pO_2 range and it causes the material to achieve a steady vacancy concentration independently on the pO_2 and $\sigma \propto [V_O^{\cdot\cdot}]$. The fact that there is not a continuous slope of -1/6 indicates that, even at pO_2 higher than 10^{-3} atm, the total conductivity should be predominantly ionic as n-type electronic conductivity would result in a continuous increase of conductivity when pO_2 decreases, not observed in the experimental results. The predominant ionic conduction agrees with the fact that electronic conductivity for Co free samples will occur with the reduction of Ce^{+4} to Ce^{+3}, and the polaron hopping in Tb sublattice, which are not likely produced in these atmospheres and temperatures.

Predominant ionic conductivity behaviour can be extended to the Co added $Ce_{0.9}Tb_{0.1}O_{2-\delta}$ sample in the studied temperature range, taking into account the ability of Co to enhance the reducibility and favour the vacancy formation at temperature above 673 K from higher pO_2. As a result, pO_2 slope is smoothed and an extended plateau range is observed. The improved conductivity is related for these Co-containing compounds to (i) the higher oxygen vacancy concentration, mainly associated to the higher Tb reducibility; (ii) the contribution of n-type electronic conductivity ascribed to the small polaron hopping through Tb^{+4}/Tb^{+3} sublattice [35] and (iii) the higher sample density and grain packing due to high sintering activity of Co-containing cerias.

As aforementioned, $Ce_{0.8}Tb_{0.2}O_{2-\delta}$ introduces more oxygen vacancies than the 10% doped material. At 673 K, pO_2 conductivity dependency is lower than -1/6 meanwhile at 1073 K the similar slope is observed but the ionic plateau is reached at pO_2 lower than 10^{-3} atm. pO_2 dependency smaller than -1/6 sets the behaviour of the material in a diffuse region between the vacancy concentration pO_2 independent and the -1/6 dependence. Therefore, the higher Tb concentration leads to higher oxygen vacancy formation and broadening of the electrolytic region over that of $Ce_{0.9}Tb_{0.1}O_{2-\delta}$.

Finally, Co addition to $Ce_{0.8}Tb_{0.2}O_{2-\delta}$ widens the ionic conductivity plateau over the whole studied pO_2 range at 1073 K and provides the highest conductivity values obtained in this study. However, a slightly positive slope is observed at 673 K, which suggests that the enhancement of vacancy formation by Co is such that causes defect interaction as is typical for highly doped specimens. The electrostatic interaction among dopant Tb^{3+} and the oppositely charged oxygen vacancy generates a new type of defect as [38,39]: $Tb'_{Ce} + V_O^{\cdot\cdot} \leftrightarrow (Tb'_{Ce}V_O^{\cdot\cdot})^{\cdot}$. These associated defects prevent oxygen vacancies to move and consequently the ionic conductivity diminishes while the activation energy rises. This effect is more appreciable at low temperatures and it does not appear at high temperatures since there is enough energy to exceed the defect dissociation barrier. Thus, oxygen vacancies are free and able to account on the ionic transport process.

3.3. Permeation measurements and stability tests

The combination of conductivity and permeation measurements using imposed current allowed determining the ambipolar conductivity at high temperature for $Ce_{0.8}Tb_{0.2}O_{2-\delta}$ + Co 2%. This compound shows electronic conductivity although ionic

conduction prevails (Figure 6). In this section, the oxygen permeation through different samples has been determined under certain pO_2 gradients and this may enable to assess the presence of mixed conductivity and the applicability as O_2 separating membranes. Oxygen permeation of $Ce_{0.9}Tb_{0.1}O_{2-\delta}$, $Ce_{0.9}Tb_{0.1}O_{2-\delta}$ + Co 2% and $Ce_{0.8}Tb_{0.2}O_{2-\delta}$ + Co 2% membranes sintered at 1473 K has been measured. Figure 8 shows the oxygen flux as a function of temperature for two sweep gases, i.e., argon and diluted methane.

Figure 8 illustrates also the flux obtained with benchmark perovskite-based membranes. $Ce_{0.9}Tb_{0.1}O_{2-\delta}$ Co-free sample showed nearly negligible permeability (not shown) and this confirms the pure ionic conductivity of this composition. However, a 0.9 and 1.2 mm-thick membranes made of $Ce_{0.9}Tb_{0.1}O_{2-\delta}$ + Co 2% and $Ce_{0.8}Tb_{0.2}O_{2-\delta}$ + Co 2% present permeation values at 1273 K around 0.02 and 0.08 $mL \cdot min^{-1} \cdot cm^2$ for argon sweeping, respectively. The O_2 flux obtained agrees perfectly with the expected value calculated[2] considering the ambipolar conductivity $\sigma_{amb} = \frac{\sigma_i \sigma_e}{(\sigma_i + \sigma_e)}$ and assuming a constant mean value in the experimental pO_2 gradient.

In more reducing conditions the permeation can be enhanced and for methane sweeping $Ce_{0.9}Tb_{0.1}O_{2-\delta}$ + Co 2% sample is able to achieve 0.5 $mL \cdot min^{-1} \cdot cm^2$. This flux increase is attributed to the substantial rise of n-type conductivity achieved preferentially through Ce^{4+} reduction. The permeation values are interesting also when compared to some perovskite type permeation membranes, especially due to the high stability under reducing and CO_2 containing atmospheres at high temperatures, where broadly-applied perovskite materials are prone to decompose. Specifically, these harsh operation conditions are encountered in the targeted applications in oxyfuel processes using flue gas as sweep and high-temperature catalytic membrane reactors for hydrocarbon conversion into syngas and added-value products. The stability of $Ce_{0.9}Tb_{0.1}O_{2-\delta}$ and $Ce_{0.9}Tb_{0.1}O_{2-\delta}$ + Co 2% has been studied by thermogravimetry under continuous flow of air with 5% CO_2. Figure 9 shows the mass evolution of this sample together with the evolution of a highly-permeable perovskite, i.e., BSCF. Carbonates are formed (mass increase) in the range from 700 to 900ºC and decompose (mass decrease) at higher temperatures, as it can be observed for the BSCF measurement.

---

[2] $j_{O2} = \frac{RT}{16F^2L} \int_{p_1}^{p_2} \frac{\sigma_i \sigma_e}{(\sigma_i + \sigma_e)} d\ lnpO_2$

e. g. at 1133 K, $j_{O2\ (experimental)} = 2.8 \cdot 10^{-8}$ $mol \cdot s^{-1} \cdot cm^{-2}$, $\sigma_{amb} = 0.0085$ $S \cdot cm^{-1}$ and $j_{O2\ (calculated)} = 3.1 \cdot 10^{-8}$ $mol \cdot s^{-1} \cdot cm^{-2}$, where $j_{O2(calculated)} = \frac{RT}{16F^2} 0.0085 ln \frac{0.21}{0.00019}$.

Ceria sample presents a negligible formation of carbonates while it is also detected the mass loss due to oxygen release at temperatures above 700K.

3.4.Conductivity relaxation study

Two important parameters characterizing mixed-conducting materials for oxygen permeation membranes are the chemical diffusion coefficient (*D*), which characterizes the diffusion kinetics of composition changes and surface exchange coefficient (*k)*. Changes in the non stoichiometry δ are related with changes in the carrier concentration. This fact is translated in macroscopic conductivity (σ) variations that can be measured by conductivity electrical relaxation technique (ECR). The relaxation process follows after an abrupt change of the oxygen partial pressure that produces a change in stoichiometry of the oxide. It is possible to measure the way back to the equilibrium by monitoring the conductivity and thus estimate values of *D* and *k*. In oxygen deficient oxides a change in pO_2 induces an oxygen vacancy excess or deficit at the surface. The vacancies then diffuse into or out of the solid to recover thermodynamic equilibrium.

The oxygen exchange kinetics of $Ce_{0.9}Tb_{0.1}O_{2-\delta}$ +Co has been investigated by alternatively swapping oxygen partial pressure from 1 to 0.21 atm at some given temperatures. The conductivity change is reproducible and reversible, and slightly faster in the oxidation direction as shown in Figure 10a. As the measured process is not surface exchange reaction limited, thickness of the sample is a parameter affecting to the relaxation time. Short relaxation time (≈300 s) is due to the thin thickness of the specimen.

D and *k* parameters were determined by numerical fitting of the relaxation curves to the diffusion model described in equation (3) and are represented in Figure 10b as a function of the inverse temperature. *D* is in the range 10^{-5} - 10^{-4} cm^2/s and *k* 10^{-4} - 10^{-3} cm/s from 773-1023 K. Arrhenius plots on Figure 5b indicate that both diffusion and surface exchange processes are thermally activated. The activation energies are 0.17 eV for *k* and 0.22 eV for *D* as obtained by linear regression analysis.

The obtained *D* and *k* values are similar or even higher than those reported for highly oxygen-permeable and catalytic membrane materials based on perovskites. Specifically, $La_{0.6}Sr_{0.4}Co_{0.2}Fe_{0.8}O_{3-\delta}$ (LSCF) measured by Lane and Kilner [40]

delivered values of $D=10^{-5}$ cm^2/s and $k=2\cdot10^{-4}$ cm/s at 1073 K and similar pO_2. $Ba_{0.5}Sr_{0.5}Co_{0.8}Fe_{0.2}O_{3-\delta}$ showed [41] values of $D= 2\cdot10^{-5}$ cm^2/s and $k=2\cdot10^{-3}$ cm/s at 1023 K. There are only few published studies on conductivity relaxation of lanthanide doped ceria. The results of this study are in good agreement with the estimations of Yashiro et al [42] for 10% gadolinium doped ceria (CGO). They reported an ECR assessment under high oxygen partial pressure conditions of $D=2.5\cdot10^{-4}$ cm^2/s at 1073 K. Specially remarkable is the relatively high k value obtained for $Ce_{0.9}Tb_{0.1}O_{2-\delta}$ +Co, which confirms the high catalytic activity for oxygen activation. As a consequence, $Ce_{1-x}Tb_xO_{2-\delta}$ +Co based membrane materials show a promising combination of high catalytic activity, high oxygen-ion diffusivity, stability under realistic operation conditions and sufficient mixed conductivity to achieve reasonable oxygen flux. From the present results, it is reasonable to assert that high permeation and robust membrane operation could be achieved by (i) proper fine-tuning of the membrane composition and layer microstructure and (ii) development of supported thin-films on porosity-engineered substrates.

4. Conclusions

Tb doped ceria shows predominant ionic conductivity or mixed ionic-electronic conductivity depending on the Tb and Co doping level and temperature range, which proves MIEC properties of these compounds.

Partial reduction of $Ce_{0.9}Tb_{0.1}O_{2-\delta}$ ($Tb^{4+} \rightarrow Tb^{3+}$) is achieved at temperatures beyond 750 K and $pO_2 \approx 10^{-4}$ atm. In these conditions ionic conductivity is predominant. Higher doping levels (20%) causes changes in the Tb^{4+}/Tb^{3+} ratio allowing small polaron hopping between Tb ions of different oxidation state (as the Ce does not reduce under the studied pO_2 range). As a consequence, the electronic conductivity of these compositions in oxidizing conditions is not negligible and will be limited by the number of available sites for electron hops. XRD results showed that Co addition does affect the oxidation state of Tb, increasing the ratio Tb^{4+}/Tb^{3+}. However, it is not entirely incorporated into the ceria lattice, but in the grain boundary. Consequently, the addition of cobalt oxide enables the improvement of the sintering and densification of specimens and the significant enhancement in total conductivity due to (i) the improved material reducibility at high temperatures and the associated rise in electronic conductivity and (ii) the increased concentration of oxygen vacancies. The

higher reducibility of Co-containing Tb-doped cerias is also inferred from temperature programmed oxygen desorption experiments done under helium gas flow, which showed (i) the Tb^{+4} reduction at temperatures above 700 K and (ii) Co reduction at 1050 K.

Oxygen permeation was negligible for cobalt-free samples while $Ce_{0.9}Tb_{0.1}O_{2-\delta}$ + Co and $Ce_{0.8}Tb_{0.2}O_{2-\delta}$ + Co showed an oxygen flux at 1273 K and 1 mm thickness of ca. 0.02 and 0.08 $mL \cdot min^{-1} \cdot cm^2$ for argon sweeping, respectively. This permeation values are increased until reaching values 0.5 $mL \cdot min^{-1} \cdot cm^2$ at 1273K ($Ce_{0.9}Tb_{0.1}O_{2-\delta}$ + Co sample) by using methane as sweep gas. Permeability results confirm the higher ambipolar conductivity of the $Ce_{0.8}Tb_{0.2}O_{2-\delta}$ + Co 2% composition and the possibility to achieve suitable mixed conductivity values by the appropriate dopants and doping level.

Thermogravimetric tests carried out in air with 5% CO_2 confirmed the stability of ceria material in contrast with the instability observed for Ba- and Sr-containing perovskites. The combined oxygen permeation and stability under reducing and carbonated atmospheres suggests the application of $Ce_{1-x}Tb_xO_{2-\delta}$ + Co 2% as membrane materials in catalytic membrane reactors for hydrocarbon and syngas conversion and oxygen separation using flue gas sweeping.

Conductivity relaxation allowed the determination of oxygen vacancy diffusion coefficient (D) and oxygen exchange coefficient (k) at high pO_2 conditions for $Ce_{0.9}Tb_{0.1}O_{2-\delta}$ + Co 2% mol. D varies from 10^{-5} to 10^{-4} cm^2/s and k from 10^{-4} to 10^{-3} cm/s corresponding to the temperature range 773-1023 K. These values are in agreement with reported results for $Ce_{0.9}Gd_{0.1}O_{2-\delta}$ and lay within the range for the targeted application as oxygen separation membrane.

5. Acknowledgements

Financial support by the Spanish Ministry for Science and Innovation (Project ENE2008-06302, Grant JAE-Pre 08-0058 and Grant BES-2009-015835), Spanish Industry Ministry (Project IAP-560620-2008-17), the EU through FP7 NASA-OTM Project (NMP3-SL-2009-228701) and *Instalaciones Inabensa S.A.* is kindly acknowledged.

Figure Captions:

Figure 1. XRD patterns recorded at room temperature and SEM pictures of $Ce_{1-x}Tb_xO_{2-\delta}$ and $Ce_{1-x}Tb_xO_{2-\delta}$ +Co.

Figure 2. a) Cell parameter dependence on the dopant amount, b) Grain size dependence on the cell parameter.

Figure 3. HT-XRD heating up in air (solid symbols) and cooled down in He (open symbols) of $Ce_{0.9}Tb_{0.1}O_{2-\delta}$ and $Ce_{0.9}Gd_{0.1}O_{2-\delta}$.

Figure 4. Normalized TPD measured in He of $Ce_{0.8}Tb_{0.2}O_{2-\delta}$, $Ce_{0.9}Tb_{0.1}O_{2-\delta}$, $Ce_{0.8}Tb_{0.2}O_{2-\delta}$. + Co and $Ce_{0.9}Tb_{0.1}O_{2-\delta}$.+Co. Inset: CeO_2 and CeO_2+Co. The intensity (ion current) corresponds to m/z = 32.

Figure 5. (a) Arrhenius plot of $Ce_{1-x}Tb_xO_{2-\delta}$ and b) $Ce_{1-x}Tb_xO_{2-\delta}$ + Co (2 mol %) at oxygen partial pressures of 0.21 and $5 \cdot 10^{-5}$ atm.

Figure 6: Total, ionic and electronic conductivity (a) transport numbers of $Ce_{0.8}Tb_{0.2}O_{2-\delta}$. + Co measured across a 1.2 mm thick membrane under a nominal gradient of pO_2 0.21 || $5x10^{-5}$ atm (air/Ar). $J(O_2)$ measured using chromatography analytical data.

Figure 7. Conductivity of $Ce_{1-x}Tb_xO_{2-\delta}$ system as a function of oxygen partial pressure measured at 673 K (a) and 1073 K (b).

Figure 8. Oxygen permeation flux as a function of inverse temperature for $Ce_{0.9}Tb_{0.1}O_{2-\delta}$ + Co 2% and $Ce_{0.8}Tb_{0.2}O_{2-\delta}$ + Co 2% (a)

Figure 9. Thermogravimetric analysis under CO_2 flow of $Ce_{1-x}Tb_xO_{2-\delta}$ / $Ce_{1-x}Tb_xO_{2-\delta}$ + Co 2% in CO_2, and $Ba_{1-x}Sr_xCo_{0.8}Fe_{0.2}O_{3-\delta}$

Figure 10. Experimental relaxation curve in the form of conductivity change versus time from pO_2= 1 atm to 0.21 atm (left-hand), and chemical diffusion coefficient and surface exchange coefficient (right-hand) as a function of temperature for $Ce_{0.9}Tb_{0.1}O_{2-\delta}$ + 2% Co.

Table 1. Apparent activation energies in the temperature range of 1073-750 K and 750-673 K and conductivities at 1073 K under air and $5x10^{-5}$ atm.

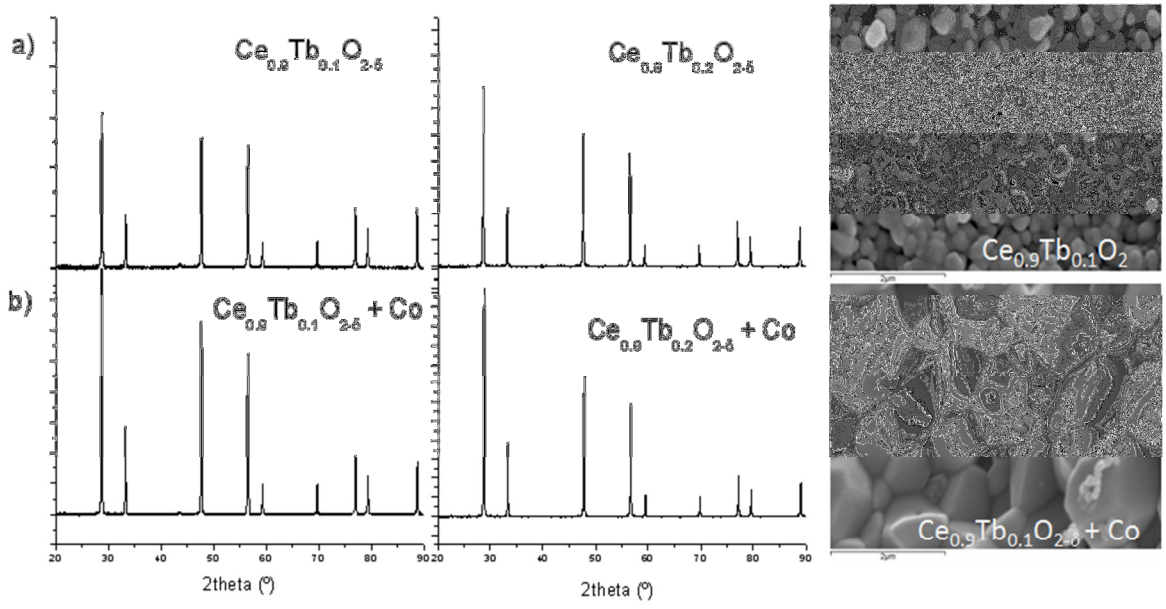
a)
$Ce_{0.9}Tb_{0.1}O_{2-\delta}$
$Ce_{0.8}Tb_{0.2}O_{2-\delta}$
b)
$Ce_{0.9}Tb_{0.1}O_{2-\delta}$ + Co
$Ce_{0.8}Tb_{0.2}O_{2-\delta}$ + Co
20 30 40 50 60 70 80 90
2theta (°)
20 30 40 50 60 70 80 90
2theta (°)
$Ce_{0.9}Tb_{0.1}O_2$
$Ce_{0.9}Tb_{0.1}O_{2-\delta}$ + Co

Figure 1

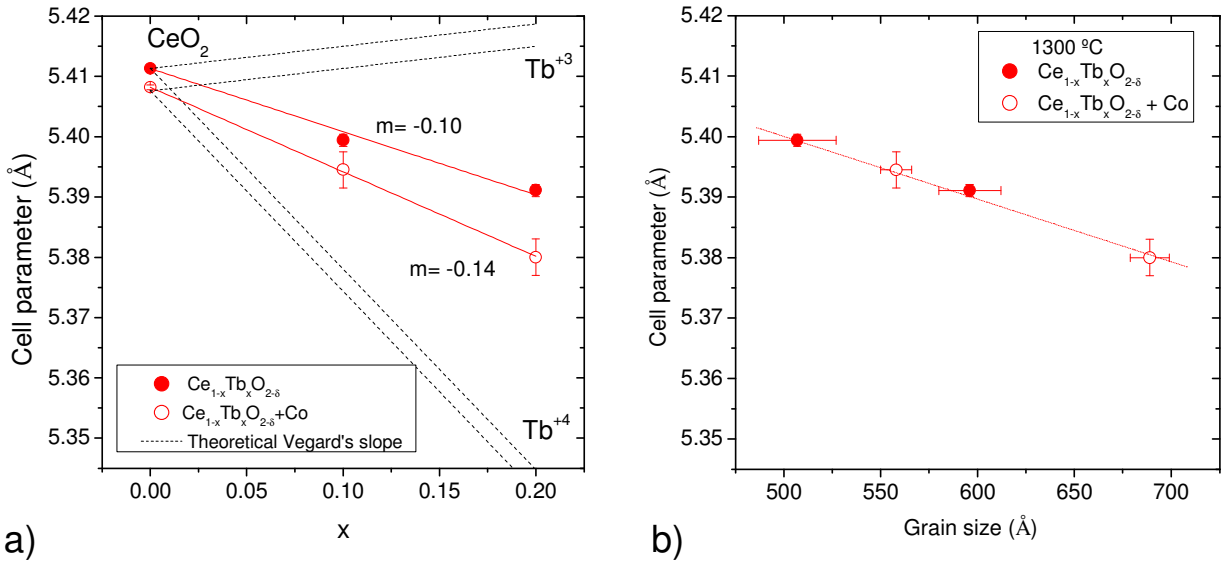
CeO2
Tb+3
Tb+4
m= -0.10
m= -0.14
Ce1-xTbxO2-δ
Ce1-xTbxO2-δ+Co
Theoretical Vegard's slope
Cell parameter (Å)
x
a)
1300 ºC
Ce1-xTbxO2-δ
Ce1-xTbxO2-δ + Co
Cell parameter (Å)
Grain size (Å)
b)

Figure 2

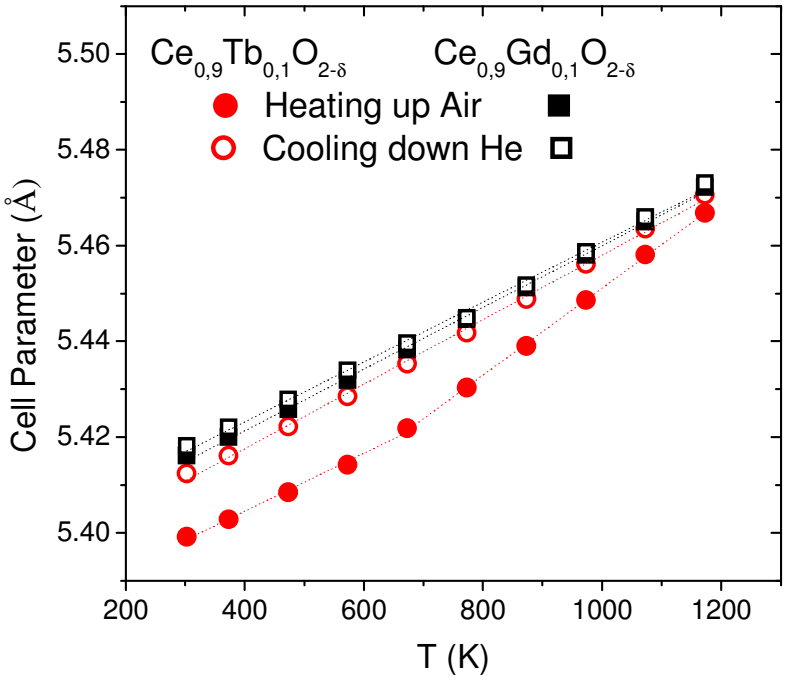
Ce0,9Tb0,1O2-δ
Ce0,9Gd0,1O2-δ
Heating up Air
Cooling down He
Cell Parameter (Å)
T (K)
5.50
5.48
5.46
5.44
5.42
5.40
200
400
600
800
1000
1200

Figure 3

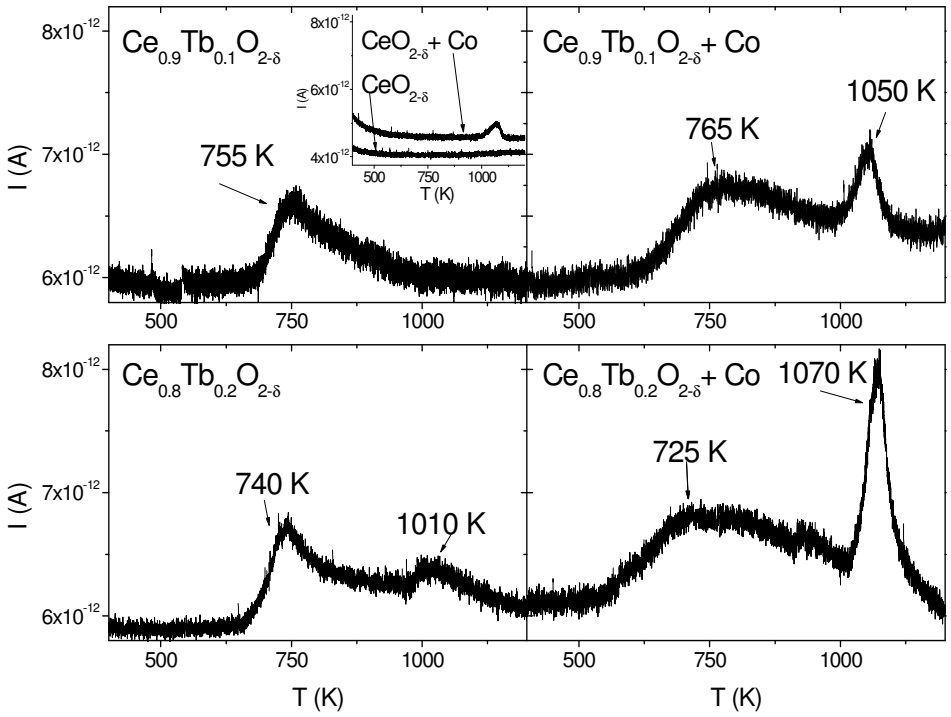
Ce0.9Tb0.1O2-δ
755 K
CeO2-δ + Co
CeO2-δ
Ce0.9Tb0.1O2-δ + Co
765 K
1050 K
Ce0.8Tb0.2O2-δ
740 K
1010 K
Ce0.8Tb0.2O2-δ + Co
725 K
1070 K
I (A)
T (K)

.

Figure 4

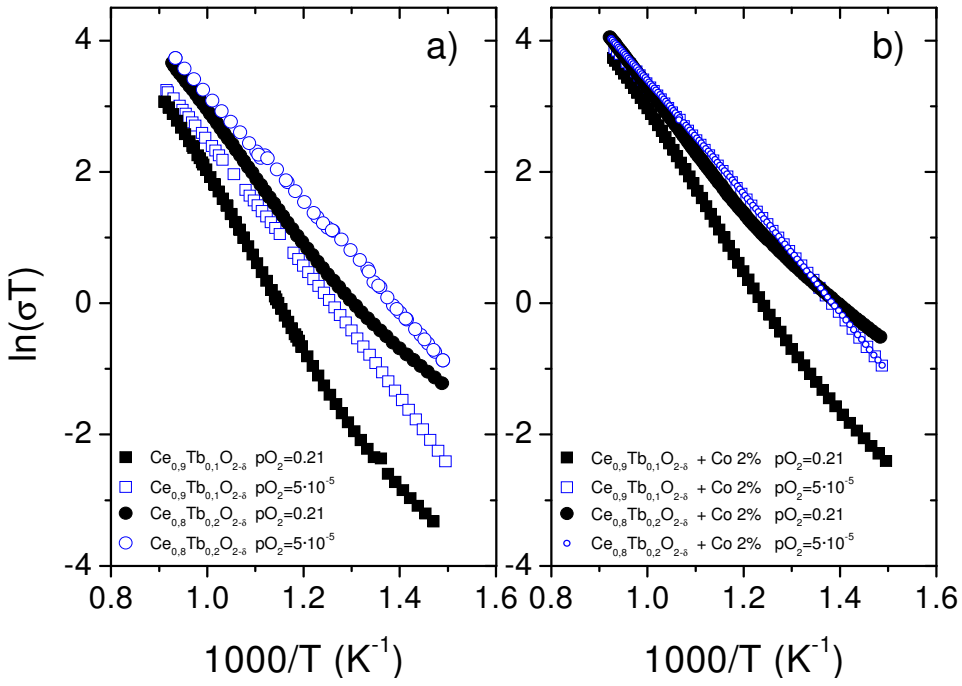
a)
b)
ln(σT)
1000/T (K-1)
1000/T (K-1)
Ce0,9Tb0,1O2-δ pO2=0.21
Ce0,9Tb0,1O2-δ pO2=5·10-5
Ce0,8Tb0,2O2-δ pO2=0.21
Ce0,8Tb0,2O2-δ pO2=5·10-5
Ce0,9Tb0,1O2-δ + Co 2% pO2=0.21
Ce0,9Tb0,1O2-δ + Co 2% pO2=5·10-5
Ce0,8Tb0,2O2-δ + Co 2% pO2=0.21
Ce0,8Tb0,2O2-δ + Co 2% pO2=5·10-5

Figure 5

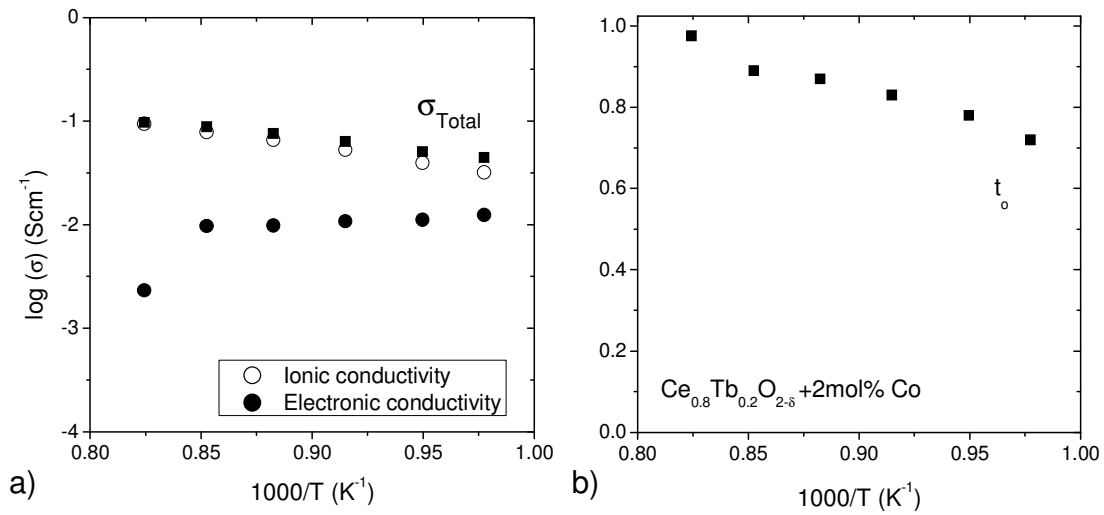
a)
log (σ) (Scm-1)
1000/T (K-1)
σTotal
Ionic conductivity
Electronic conductivity
b)
1000/T (K-1)
to
Ce0.8Tb0.2O2-δ +2mol% Co

Figure 6

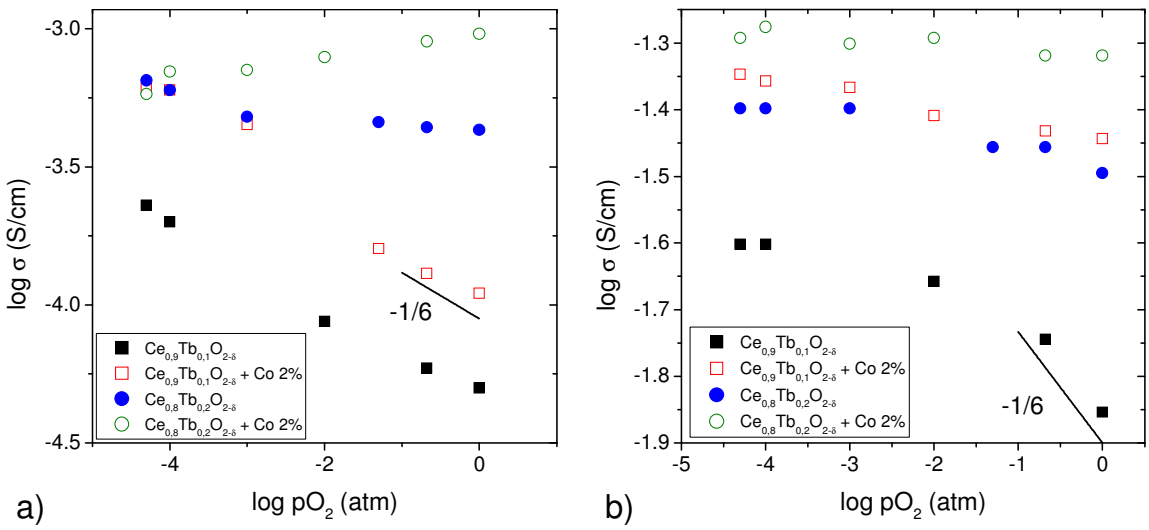
log σ (S/cm)
log pO2 (atm)
-1/6
Ce0,9Tb0,1O2-δ
Ce0,9Tb0,1O2-δ + Co 2%
Ce0,8Tb0,2O2-δ
Ce0,8Tb0,2O2-δ + Co 2%
a)
b)

Figure 7

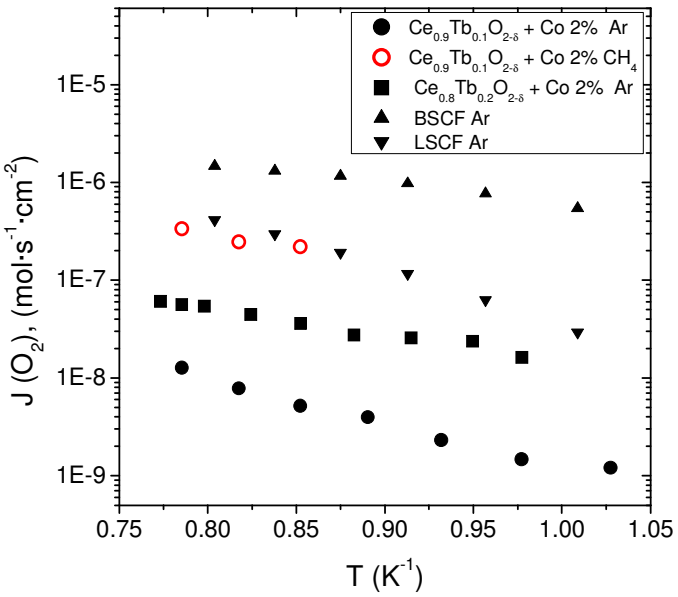
Ce0.9Tb0.1O2-δ + Co 2% Ar
Ce0.9Tb0.1O2-δ + Co 2% CH4
Ce0.8Tb0.2O2-δ + Co 2% Ar
BSCF Ar
LSCF Ar
1E-5
1E-6
1E-7
1E-8
1E-9
J (O2), (mol·s-1·cm-2)
0.75
0.80
0.85
0.90
0.95
1.00
1.05
T (K-1)

Figure 8

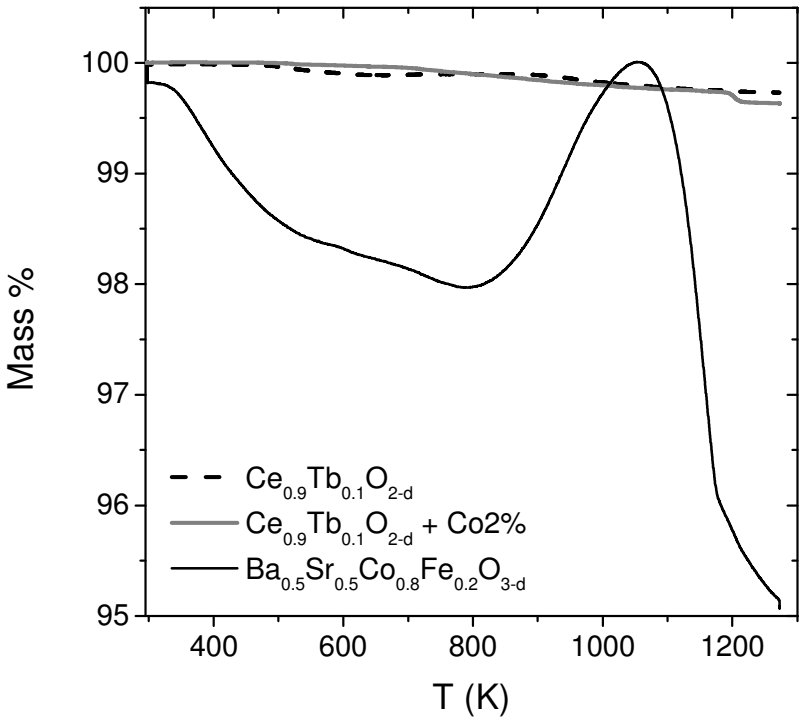
100
99
98
97
96
95
Mass %
400
600
800
1000
1200
T (K)
Ce0.9Tb0.1O2-d
Ce0.9Tb0.1O2-d + Co2%
Ba0.5Sr0.5Co0.8Fe0.2O3-d

Figure 9

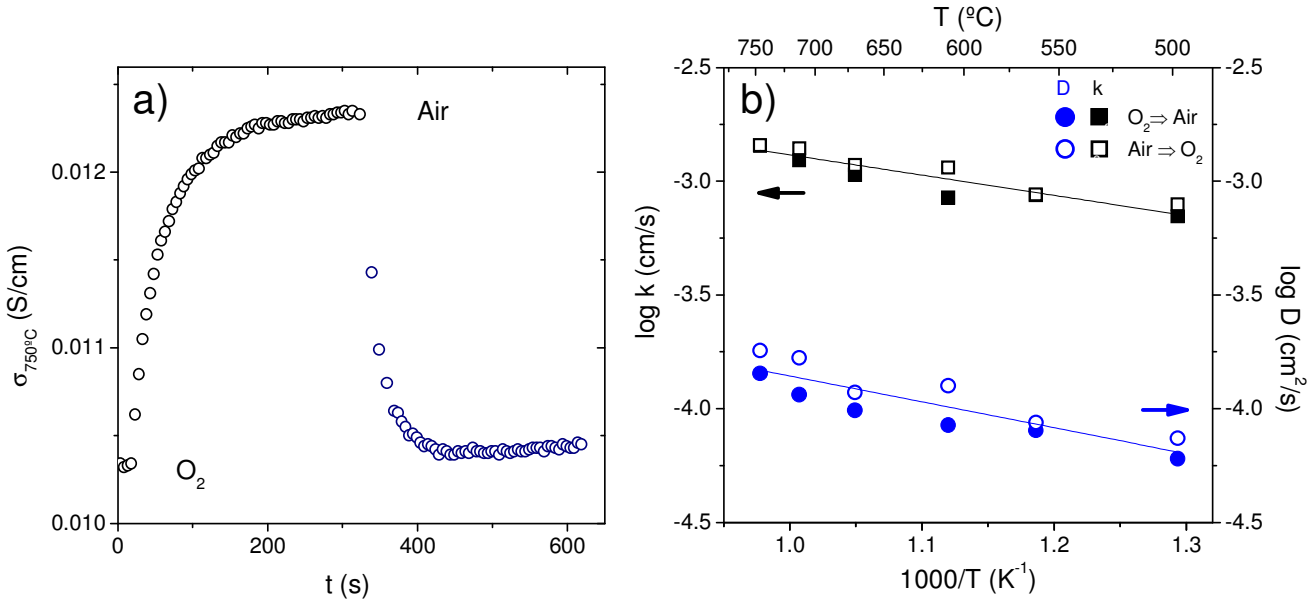
a)
Air
O2
0.012
0.011
0.010
σ750ºC (S/cm)
0
200
400
600
t (s)
T (ºC)
750
700
650
600
550
500
b)
D
k
O2⇒ Air
Air ⇒ O2
-2.5
-3.0
-3.5
-4.0
-4.5
log k (cm/s)
log D (cm2/s)
1.0
1.1
1.2
1.3
1000/T (K-1)

Figure 10

	E_a (eV)			σ (S/cm) 1073 K	
	0.21 atm		$5x10^{-5}$ atm	0.21 atm	$5x10^{-5}$ atm
	High T	Low T			
$Ce_{0.9}Tb_{0.1}O_{2-\delta}$	1.08	0.67	0.80	0.018	0.025
$Ce_{0.9}Tb_{0.1}O_{2-\delta}$ + Co 2%	1.06	0.76	0.75	0.038	0.045
$Ce_{0.8}Tb_{0.2}O_{2-\delta}$	0.87	0.59	0.71	0.035	0.040
$Ce_{0.8}Tb_{0.2}O_{2-\delta}$ + Co 2%	0.82	0.55	0.77	0.048	0.051

Table 1

Supporting Information Available: Additional TPR results of the samples are plotted in figure S1. Oxygen flux measurements under different temperatures as a function of imposed current are depicted in figure S2. Figure S3 shows OCV measurements compared with Nernst theoretical values. OCV values are lower than theoretical, which indicates that a electronic component exists.

María Balaguer, Cecilia Solís, José M. Serra*

Graphical Summary

Study of the transport properties of the mixed ionic electronic conductor $Ce_{1-x}Tb_xO_{2-\delta}$ + Co (x=0.1, 0.2) and evaluation as oxygen-transport membrane

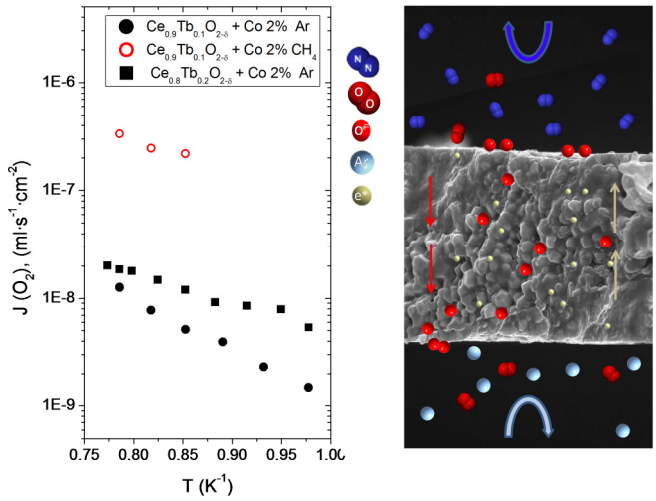

SUPPORTING INFORMATION

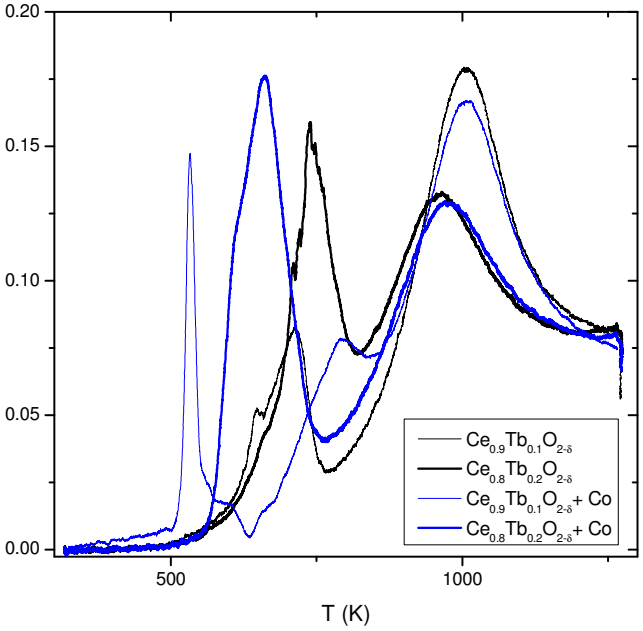

S1. H_2 TPR for $Ce_{1-x}Tb_xO_{2-\delta}$ and $Ce_{1-x}Tb_xO_{2-\delta}$ + Co 2mol%.

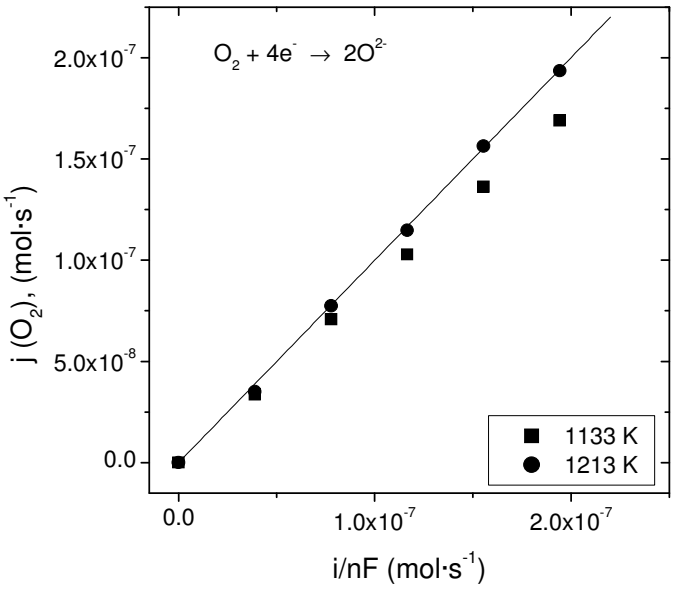

S2. Oxygen flux under different temperatures as a function of imposed current for a $Ce_{0.8}Tb_{0.2}O_{2-\delta}$ + Co 2mol% membrane.

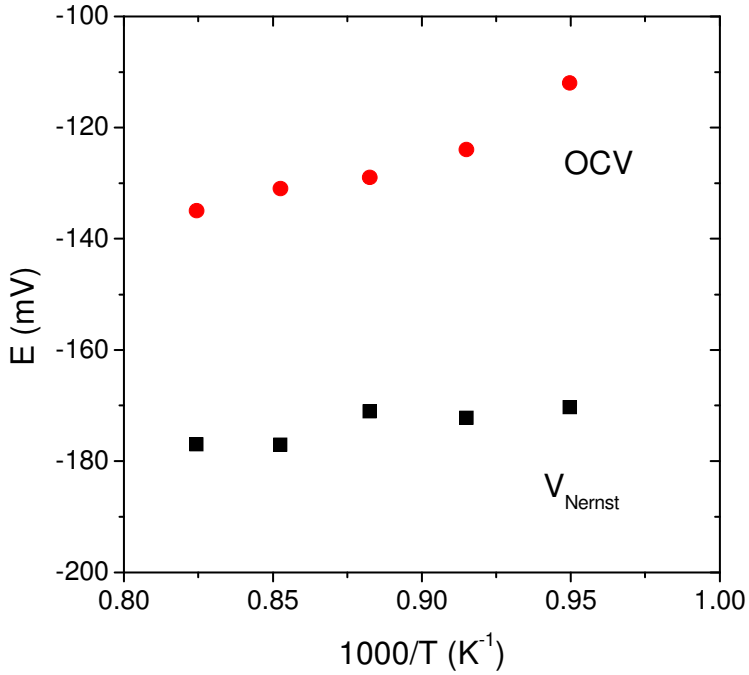

S3. OCV measurements and Nernst theoretical values for a $Ce_{0.8}Tb_{0.2}O_{2-\delta}$ + Co 2mol% membrane.

References

1 Engels S.; Beggel F.; Modigell M.; Stadler H. *J. Membr. Sci.* **2010,** 90, 93.

2 Toftegaard M.B.; Brix J.; Jensen P.A.; Glarborg P.; Jensen A.D. *Prog. Energy and Combustion Sci.* **2010**, 36, 581.

3 Bouwmeester H. J. M. *Catal. Today* **2003**, 82, 141.

4 Jiang H.Q.; Cao Z.W.; Schirmeister S.; Schiestel T.; Caro J.; *Angew. Chem. Int.* **2010**, 46, 5656.

5 Jiang H.Q.; Xing L.; Czuprat O.; Wang H.H.; Schirmeister S.; Schiestel T.; Caro J. *Chem. Comm.* **2009**, 44, 6738.

6 Smart S.; Lin C.X.C.; Ding L.; Thambimuthu K.; da Costa J. C. D., *Energy Environ. Sci.* **2010**, 3, 268.

7 Slade D.A.; Jiang Q.Y.; Nordheden K. J.; Stagg-Williams S. M.; *Catal. Today* **2009**, 148, 290.

8 Sunarso J.; Baumann S.; Serra J.M.; Meulenberg W.A.; Liu S.; Lin Y.S.; Diniz da Costa J.C. *J. Membr. Sci.* **2008**, 320, 13.

9 Fontaine M. L.; Larring Y.; Norby T.; Grande T.; Bredesen R.; *Annales de Chim. Sci. Mat*. **2007**, 32, 197.

10 Serra J.M.; Vert V. B.; Büchler O.; Meulenberg W. A.; Buchkremer H. P. *Chem. Mater.* 2008, 20, 3867.

11 Chen Z.;Ran Ran; Shao Z.; Yu H.; Diniz da Costa J.C.; Liu S., *Ceram. Int.* **2009**, 35, 2455.

12 Kusaba H.; Shibata Y.; Sasaki K.; Teraoka Y., *Solid State Ionics* **2006**, 177, 2249.

13 Leo A., Smart S., Liu S., Diniz da Costa J. C., *J. Membr. Sci,* **2011,** 368, 64

14 Liu S., Tan Shao X., Diniz da Costa J. C., *AIChe*, **2006**, 52, 3452

15 Arnold M.; Wang H.; Feldhoff A.; *J. Membr. Sci.* **2007**, 293, 44.

16 Shao Z. P.; Yang W. S., Cong Y.; Dong H.; Tong J. H.; Xiong G. X.; *J. Membr. Sci.* **2000**,172, 177.

17 Leo A.; Liu S.; da Costa J. *Int. J. Greenhouse Gas Control* **2009**, 3, 357.

18 Park J. H.; Kim J. P.; Son S. H. *Energy Procedia* **2008**, 1, 369.

19 Fagg D.P.; Shaula A.L.; Kharton V.V.; Frade J.R. *J. Membr. Sci.* **2007**, 299,1.

20 Chatzichristodoulou C.; Hendriksen P.V.; Hagen A.; Grivel J.C. *ECS Transactions* **2008**, 13, 347.

21 Shaula A.L.; Kharton V.V.; Marques F.M.B.; Kovalevsky A.V.; Viskup A.P.; Naumovich E.N. *J Solid State Electrochem* **2006**, 10, 28.

22 Kumar A.; Babu S.; Karakoti A.S.; Schulte A.; Seal S. *Langmuir* **2009**, 25,10998.

23 Song C.R.; Yoo H.I. *Solid State Ionics* **1999**, 124, 289.

24 Søgaard M.; Van Hendriksen P.; Mogensen M. *J. Solid State Chem.* **2007**, 180, 1489.

25 Kim D.-J. *J. Am. Ceram. Soc.* **1989**, 72, 1415.

26 Nicholas J.D.; De Jonghe L.C. *Solid State Ionics* **2007**, 178, 1187.

27 Ayawanna J., Wattanasiriwech D., Wattanasiriwech S, Aungkavattana P. *Solid State Ionics* **2009**, 180, 1388.

28 Hong S.J.; Virkar A.V. *J. Am. Ceram. Soc.* **1995**, 78, 433.

29 Mogensen M.; Sammes N.M.; Tompsett G.A. *Solid State Ionics* **2000**, 129, 63.

30 Tang C.-W, Wang C.-B., Chien S.-H., *Thermochimica Acta* **2008**, 43, 68.

31 Chatzichristodoulou C.; Hendriksen P.V.; Hagen A. *J. Electrochem. Soc.* **2010**, 157, B299.

32 Tsunekawa S.; Ishikawa K.; Li Z.-Q.; Kawazoe Y.; Kasuya A. *Phys. Rev. Lett.* **2000**, 85, 3440.

33 Zhou X.-D.;Huebner W. *Appl. Phys Lett.* **2001**, 79, 3512.

34 Kosacki I.; Suzuki T.; Anderson H.U.; Colomban P. *Solid State Ionics* **2002**, 149, 99.

35 Fagg D.P.; García-Martín S.; Kharton V.V.; Frade J.R. *Chem. Mater.* **2009**, 21, 381.

36 Fagg D.P.; Marozau I.P.; Shaula A.L.; Kharton V.V.; Frade J.R. *J. Solid State Chem.* **2006**, 179, 3347.

37 Duncan K.L.; Wang Y.; Bishop S.R.; Ebrahimi F.; Wachsman E.D. *J. Appl. Phys.* **2007**, 101, 044906.

38 Stefanik T.S.; Tuller H.L. *J. Eur. Ceram. Soc.* **2001**, 21, 1967.

39 Solís C.; Jung W.C.; Tuller H.; Santiso J. *Chem. Mater.* **2010**, 22, 1452.

40 Lane J.A.; Kilner J.A. *Solid State Ionics* **2000**, 136, 997.

41 Girdauskaite E.; Ullmann H.; Vashook V.V.; Guth U.; Caraman G.B.; Bucher E.; Sitte W. *Solid State Ionics* **2008**, 179, 385.

42 Yashiro K.; Onuma S.; Kaimai A.; Nigara Y., Kawada T.; Mizusaki J.; Kawamura K.; Horita T.; Yokokawa H. *Solid State Ionics* **2002**, 152, 469.